Universal Digital Quantum Simulation with Trapped Ions

B. P. Lanyon, *et al.*

Science **334**, 57 (2011);
DOI: 10.1126/science.1208001

when subducted lithosphere entered the shallow lower mantle and stagnated because of density inversion and increased mantle viscosity (*14*, *27*) (Fig. 3B). If heated to ambient mantle temperatures, carbonated basaltic lithologies form carbonated melts, which can then be reduced to diamond during reactions with surrounding mantle (*8*, *28*). Our results also indicate that the diamonds were transported by convection from the lower to the upper mantle, where the originally homogeneous inclusions unmixed. For example, phase relations along the $NaAlSiO_4$-$MgAl_2O_4$ boundary (*29*) indicate that the bulk composition of inclusion Ju5-20 would yield the observed assemblage of nepheline plus spinel (Fig. 1A and fig. S1B) at depths of ~150 km; other inclusions in diamonds from the Juina region (*3*, *4*, *8*) also suggest equilibration near the base of the Brazilian lithosphere (~150 to 200 km). Thus, the diamonds record a history of upward transport on the order of 500 to 1000 km or more before being sampled by a Cretaceous kimberlite and brought to the surface.

On the basis of seismological and petrological evidence, previous workers have argued for a mantle plume beneath Brazil during the Cretaceous (*30*, *31*). Furthermore, paleo-plate reconstructions show that the Juina region of Brazil was located at the margin of the African large low shear velocity provinces during the Cretaceous, which may be indicative of the presence of deep mantle plumes (*32*). We suggest that some portion of stagnated subducted lithosphere in which the diamonds grew was transported from the lower mantle to the base of the Brazilian lithosphere in a rising mantle plume (Fig. 3B). The Juina-5 diamonds and their inclusions provide compelling evidence for deep cycling of oceanic crust and surface carbon into the lower mantle and, ultimately, exhumation back to the upper mantle and Earth's surface.

References and Notes

1. T. Stachel, G. P. Brey, J. W. Harris, *Elements* **1**, 73 (2005).
2. B. Harte, *Mineral. Mag.* **74**, 189 (2010).
3. G. P. Bulanova *et al.*, *Contrib. Mineral. Petrol.* **160**, 489 (2010).
4. B. Harte, N. Cayzer, *Phys. Chem. Miner.* **34**, 647 (2007).
5. F. V. Kaminsky *et al.*, *Contrib. Mineral. Petrol.* **140**, 734 (2001).
6. T. Stachel, G. P. Brey, J. W. Harris, *Contrib. Mineral. Petrol.* **140**, 1 (2000).
7. R. Tappert *et al.*, *Geology* **33**, 565 (2005).
8. M. J. Walter *et al.*, *Nature* **454**, 622 (2008).
9. R. Tappert *et al.*, *Geology* **37**, 43 (2009).
10. P. Cartigny, *Elements* **1**, 79 (2005).
11. B. Harte, J. W. Harris, M. T. Hutchison, G. R. Watt, M. C. Wilding, in *Mantle Petrology: Field Observations and High Pressure Experimentation*, Y. Fei, C. M. Bertka, B. O. Mysen, Eds. Geochemical Society Special Publications, 125 (1999).
12. P. C. Hayman, M. G. Kopylova, F. V. Kaminsky, *Contrib. Mineral. Petrol.* **140**, 734 (2005).
13. T. Stachel, J. W. Harris, G. P. Brey, W. Joswig, *Contrib. Mineral. Petrol.* **140**, 16 (2000).
14. Y. Fukao, M. Obayashi, T. Nakakuki, Deep Slab Project Group, *Annu. Rev. Earth Planet. Sci.* **37**, 19 (2009).
15. R. D. van der Hilst, S. Widiyantoro, E. R. Engdahl, *Nature* **386**, 578 (1997).
16. K. Hirose, N. Takafuji, N. Sata, Y. Ohishi, *Earth Planet. Sci. Lett.* **237**, 239 (2005).
17. S. Ono, E. Ito, T. Katsura, *Earth Planet. Sci. Lett.* **190**, 57 (2001).
18. A. Ricolleau *et al.*, *J. Geophys. Res.* **115**, (B8), B08202 (2010).
19. L. Heaman, N. A. Teixeira, L. Gobbo, J. C. Gaspar, U-Pb mantle zircon ages for kimberlites from the Juina and Paranatinga Provinces, Brazil. Extended Abstracts, 7th International Kimberlite Conference, Cape Town, South Africa, 322 (1998).
20. See supporting material on *Science* Online.
21. F. E. Brenker *et al.*, *Earth Planet. Sci. Lett.* **236**, 579 (2005).
22. F. Brenker, T. Stachel, J. W. Harris, *Earth Planet. Sci. Lett.* **198**, 1 (2002).
23. B. J. Wood, *Earth Planet. Sci. Lett.* **174**, 341 (2000).
24. M. B. Kirkley, J. J. Gurney, M. L. Otter, S. J. Hill, L. R. M. Daniels, *Appl. Geochem.* **6**, 477 (1991).
25. S. Shilobreeva, I. Martinez, V. Busigny, P. Agrinier, C. Laverne, *Geochim. Cosmochim. Acta* **75**, 2237 (2011).
26. S. Poli, E. Franzolin, P. Fumagalli, A. Crottini, *Earth Planet. Sci. Lett.* **278**, 350 (2009).
27. S. Goes, F. A. Capitanio, G. Morra, *Nature* **451**, 981 (2008).
28. A. Rohrbach, M. W. Schmidt, *Nature* **472**, 209 (2011).
29. M. Akaogi, A. Tanaka, M. Kobayashi, N. Fukushima, T. Suzuki, *Phys. Earth Planet. Inter.* **130**, 49 (2002).
30. S. A. Gibson, R. N. Thompson, O. H. Leonardos, A. P. Dickin, G. J. Mitchell, *J. Petrol.* **36**, 89 (1995).
31. J. C. VanDecar, D. E. James, M. Assumpcao, *Nature* **378**, 25 (1995).
32. T. H. Torsvik, K. Burke, B. Steinberger, S. J. Webb, L. D. Ashwal, *Nature* **466**, 352 (2010).
33. Y. N. Palyanov, Y. M. Borzdov, A. F. Khokhryakov, I. N. Kupriyanov, N. V. Sobolev, *Earth Planet. Sci. Lett.* **250**, 269 (2006).

Acknowledgments: We thank I. Buisman and S. Kearns for assisting in the collection of electron microprobe data and L. Gobbo on behalf of Rio Tinto for providing samples. Supported by UK Natural Environment Research Council grant NE/H011242/1 (M.J.W.) and NSF grant EAR-1049992 (S.B.S. and J.W.). See (*20*) for additional compositional data on inclusion phases, experimental run products, and Raman spectroscopy.

Supporting Online Material

www.sciencemag.org/cgi/content/full/science.1209300/DC1
Materials and Methods
SOM Text
Figs. S1 to S3
Tables S1 to S5
References (*34*–*45*)

3 June 2011; accepted 22 August 2011
Published online 15 September 2011;
10.1126/science.1209300

REPORTS

Universal Digital Quantum Simulation with Trapped Ions

B. P. Lanyon,[1,2]* C. Hempel,[1,2] D. Nigg,[2] M. Müller,[1,3] R. Gerritsma,[1,2] F. Zähringer,[1,2] P. Schindler,[2] J. T. Barreiro,[2] M. Rambach,[1,2] G. Kirchmair,[1,2] M. Hennrich,[2] P. Zoller,[1,3] R. Blatt,[1,2] C. F. Roos[1,2]

A digital quantum simulator is an envisioned quantum device that can be programmed to efficiently simulate any other local system. We demonstrate and investigate the digital approach to quantum simulation in a system of trapped ions. With sequences of up to 100 gates and 6 qubits, the full time dynamics of a range of spin systems are digitally simulated. Interactions beyond those naturally present in our simulator are accurately reproduced, and quantitative bounds are provided for the overall simulation quality. Our results demonstrate the key principles of digital quantum simulation and provide evidence that the level of control required for a full-scale device is within reach.

Although many natural phenomena are accurately described by the laws of quantum mechanics, solving the associated equations to calculate properties of physical systems, i.e., simulating quantum physics, is in general thought to be very difficult (*1*). Both the number of parameters and differential equations that describe a quantum state and its dynamics grow exponentially with the number of particles involved. One proposed solution is to build a highly controllable quantum system that can efficiently perform the simulations (*2*). Recently, quantum simulations have been performed in several different systems (*3*–*13*), largely following the analog approach (*2*) whereby an analogous model is built, with a direct mapping between the state and dynamics of the simulated system and those of the simulator. An analog simulator is dedicated to a particular problem, or class of problems.

A digital quantum simulator (*2*, *14*–*16*) is a precisely controllable many-body quantum system on which a universal set of quantum operations (gates) can be performed, i.e., a quantum computer (*17*). The simulated state is encoded in a register

[1]Institut für Quantenoptik und Quanteninformation, Österreichische Akademie der Wissenschaften, Otto-Hittmair-Platz 1, A-6020 Innsbruck, Austria. [2]Institut für Experimentalphysik, University of Innsbruck, Technikerstr. 25, A-6020 Innsbruck, Austria. [3]Institut für Theoretische Physik, University of Innsbruck, Technikerstr. 25, A-6020 Innsbruck, Austria.

*To whom correspondence should be addressed. E-mail: ben.lanyon@uibk.ac.at

of quantum information carriers, and the dynamics are approximated with a stroboscopic sequence of quantum gates. In principle, it can be reprogrammed to efficiently simulate any local quantum system (*14*) and is therefore referred to as a universal quantum simulator. Furthermore, there are known methods to efficiently correct for and quantitatively bound experimental error in large-scale digital simulations (*18*).

We report on digital simulations using a system of trapped ions. We focus on simulating the full time evolution of networks of interacting spin-1/2 particles, which are models of magnetism (*19*) and exhibit rich dynamics. We do not use error correction, which has been demonstrated separately in our system (*20*) and must be included in a full-scale fault-tolerant digital quantum simulator.

The central goal of a quantum simulation is to calculate the time-evolved state of a quantum system $\psi(t)$. In the case of a time-independent Hamiltonian H, the form of the solution is $\psi(t) = e^{-iHt/\hbar}\psi(0) = U\psi(0)$. A digital quantum simulator can solve this equation efficiently for any local quantum system (*14*), i.e., where H contains a sum of terms H_k that operate on a finite number of particles, owing to interaction strengths that fall off with distance, for example. In this case the local evolution operators $U_k = e^{-iH_k t/\hbar}$ can be approximated with a fixed number of operations from a universal set. However, these terms do not generally commute $U \neq \prod_k e^{-iH_k t/\hbar}$. This can be overcome with the Trotter approximation (*14*, *21*), $e^{-iHt/\hbar} = \lim_{n\to\infty}(\prod_k e^{-iH_k t/n\hbar})^n$, for integer n, which is at the heart of the digital quantum simulation algorithm. For finite n, the Trotter error is bounded and can be made arbitrarily small. The global evolution of a quantum system can therefore be approximated by a stroboscopic sequence of many small time-steps of evolution, generated by the local interactions present in the system. The digital algorithm can also be applied to time-dependent Hamiltonians and open quantum systems (*14*, *16*, *17*, *22*).

Our simulator is based on a string of electrically trapped and laser-cooled calcium ions (*23*). The $|S_{1/2}\rangle = |1\rangle$ and $|D_{5/2}\rangle = |0\rangle$ Zeeman states encode a qubit in each ion. Simulated states are encoded in these qubits and manipulated by laser pulses that implement the operation set: $O_1(\theta,j) = \exp(-i\theta\sigma^j{}_z)$; $O_2(\theta) = \exp(-i\theta\sum_j \sigma_z^j)$; $O_3(\theta,\phi) = \exp(-i\theta\sum_j \sigma_\phi{}^j)$; $O_4(\theta,\phi) = \exp(-i\theta\sum_{i<j}\sigma^i{}_\phi\sigma^j{}_\phi)$. Here $\sigma_\phi = \cos\phi\sigma_x + \sin\phi\sigma_y$ and $\sigma^j{}_k$ denotes the k-th Pauli matrix acting on the j-th qubit. O_4 is an effective qubit-qubit interaction mediated by a common vibrational mode of the ion string (*24*). Recent advances have seen the quality of these operations increase appreciably (*25*). For our simulations, we define dimensionless Hamiltonians $\tilde{H}$, i.e., $H = E\tilde{H}$ such that $U = e^{-iHEt/\hbar}$ and the system evolution is quantified by a unitless phase $\theta = Et/\hbar$.

We begin by simulating an Ising system of two interacting spin-1/2 particles, which is an elementary building block of larger and more complex spin models and was one of the first systems to be simulated with trapped ions following an analog approach (*6*, *26*). The Hamiltonian is given by $H_{\mathrm{Ising}} = B(\sigma^1{}_z + \sigma^2{}_z) + J\sigma^1{}_x\sigma^2{}_x$. The first bracketed term represents the interaction of each spin with a uniform magnetic field in the z direction and the second an interaction between the spins in an orthogonal direction. The interactions do not commute, giving rise to nontrivial dynamics and entangled eigenstates. Each spin is mapped directly to an ionic qubit ($|1\rangle = |\uparrow\rangle$, $|0\rangle = |\downarrow\rangle$). The dynamics are implemented with a stroboscopic sequence of O_2 and O_4 gates, representing the magnetic field and spin-spin evolution operators, respectively. We first simulate a time-independent case $J = 2B$, which couples the initial state $|\uparrow\uparrow\rangle$ to a maximally entangled superposition of $|\uparrow\uparrow\rangle$ and $|\downarrow\downarrow\rangle$ (Fig. 1A). The simulated dynamics converge closer to the exact dynamics as the digital resolution is increased. The overall simulation quality is quantified by quantum process tomography (QPT) (*27*), yielding a process fidelity of 91(1)% at the finest digital resolution used. In (*23*), we show how higher-order Trotter decompositions can be used to achieve more accurate digital approximations with fewer operations.

We now consider a time-dependent case where J increases linearly from 0 to $4B$ during a total evolution θ_t. In the limit $\theta_t \to \infty$, spins initially prepared in the paramagnetic ground state of the magnetic field ($|\uparrow\uparrow\rangle$) will evolve adiabatically into the antiferromagnetic ground state of the final Hamiltonian: an entangled superposition of the $\sum_j \sigma_x^j$ eigenstates $|\leftarrow\rightarrow\rangle_x$ and $|\rightarrow\leftarrow\rangle_x$. As a demonstration, we approximate the continuous dynamics, for $\theta_t = \pi/2$, using a stroboscopic sequence of 24 O_2 and O_4 gates and measure the populations in the σ_x basis (Fig. 1B). The evolution closely follows the exact case, and an entangled state is created [63(6)% tangle (*28*)]. Full quantum state reconstructions are performed after each digital step, yielding fidelities between the ideal digitized and measured state of at least 91(2)% and overlaps with the instantaneous ground state of no less than 91(2)%. The observed oscillation in expectation values is a diabatic effect, as excited states become populated.

More complex systems with additional spin-spin interactions in the y ("XY" model) and z

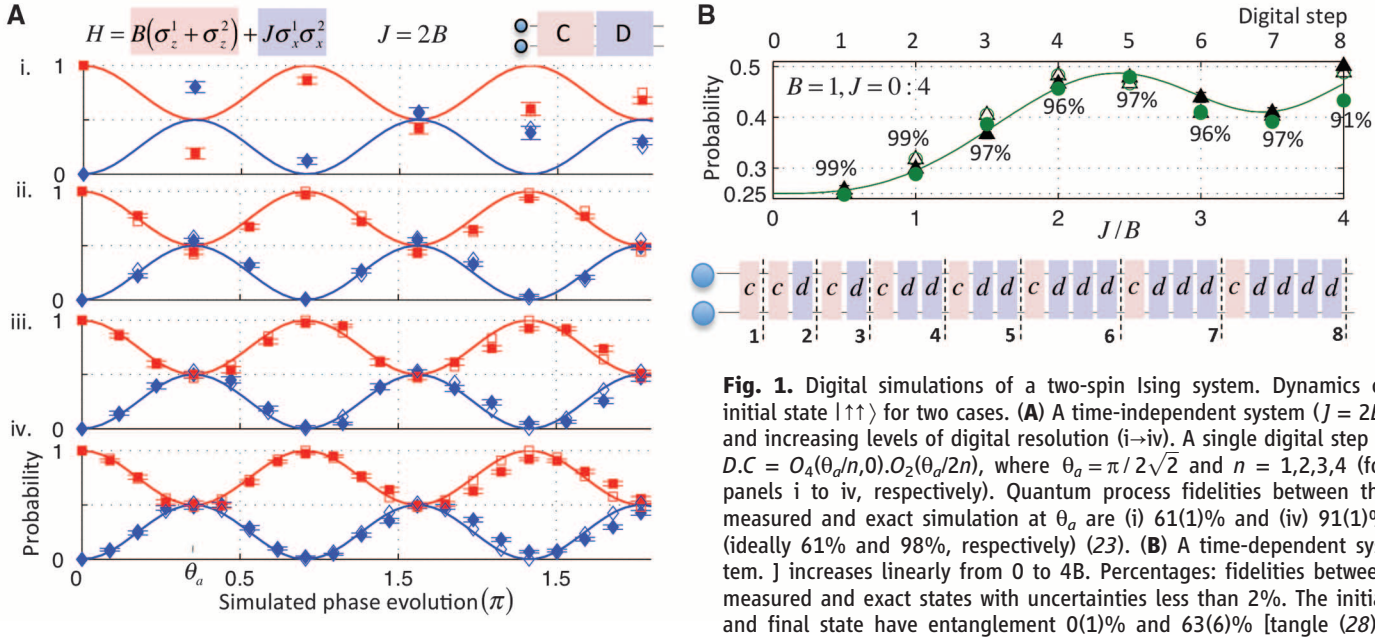

Fig. 1. Digital simulations of a two-spin Ising system. Dynamics of initial state $|\uparrow\uparrow\rangle$ for two cases. (**A**) A time-independent system ($J = 2B$) and increasing levels of digital resolution (i→iv). A single digital step is $D.C = O_4(\theta_a/n,0).O_2(\theta_a/2n)$, where $\theta_a = \pi/2\sqrt{2}$ and n = 1,2,3,4 (for panels i to iv, respectively). Quantum process fidelities between the measured and exact simulation at θ_a are (i) 61(1)% and (iv) 91(1)% (ideally 61% and 98%, respectively) (*23*). (**B**) A time-dependent system. J increases linearly from 0 to 4B. Percentages: fidelities between measured and exact states with uncertainties less than 2%. The initial and final state have entanglement 0(1)% and 63(6)% [tangle (*28*)], respectively. The digitized linear ramp is shown at the bottom: $c = O_2(\pi/16)$, $d = O_4(\pi/16,0)$. For more details, see (*23*). Lines; exact dynamics. Unfilled shapes: ideal digitized; filled shapes: data (■ ↑↑ ◆ ↓↓ ● →→$_x$ ▲ ←←$_x$).

("XYZ" model) directions can be simulated by reprogramming the operation sequence. The dynamics due to an additional spin-spin interaction in the y direction is simulated by adding another O_4 operation to each step of the Ising stroboscopic sequence (with $\phi = \pi/2$). A third spin-spin interaction in the z direction is realized by adding an O_4 gate sandwiched between a pair of O_3 operations set to rotate the reference frame of the qubits. Dynamics of the initial state $|{\rightarrow}{\leftarrow}\rangle_x$ are simulated for each model, with a fixed digital resolution of $\theta/n = \pi/16$ and up to 12 Trotter steps (Fig. 2). Up to 24, 48, and 84 gates are used for the Ising, XY, and XYZ simulations, respectively. This particular initial state is chosen because the ideal evolution is different for each model. The results show close agreement with the exact dynamics and results from QPT after four digital steps yield process fidelities, with the exact unitary evolution, of 88(1), 85(1), and 79(1)% for the Ising, XY, and XYZ, respectively. With perfect operations, the Trotter error would be less than 1% in each case. Although analog simulations of Ising models have previously been demonstrated in ion traps (*6*, *8*), XY and XYZ models have not.

The digital approach allows arbitrary interaction distributions between spins to be programmed. For three-spin systems, we realize various interactions that give rise to the dynamical evolutions of the initial state $|{\uparrow}{\uparrow}{\uparrow}\rangle$ (Fig. 3). Figure 3A shows a system supporting interactions between all spin pairs with equal strength, and between each spin and a transverse field. The initial state couples equally to $|{\uparrow}{\downarrow}{\downarrow}\rangle$, $|{\downarrow}{\uparrow}{\downarrow}\rangle$, and $|{\downarrow}{\downarrow}{\uparrow}\rangle$, while the strength of the field determines the amplitude and frequency of the dynamics. For the case shown ($J = 2B$), an equal superposition of the coupled states is periodically created [an entangled W state (*29*)]. Figure 3B shows how nonsymmetric interaction distributions can be programmed, with sequences of O_4 and O_1 to add spin-selective interactions. The interaction between one spin pair is dominant. Owing to this broken symmetry, one coupled state ($|{\uparrow}{\downarrow}{\downarrow}\rangle$) is populated faster than the others, yielding more complex dynamics than in the symmetric case. Figure 3C demonstrates the ability to simulate n-body interactions; specifically, $\sigma_z^1\sigma_x^2\sigma_x^3$. A clear signature is observed: direct coupling between $\sum_j \sigma_y^j$ eigenstates $|{\rightarrow}{\rightarrow}{\rightarrow}\rangle_y$ and $|{\leftarrow}{\leftarrow}{\leftarrow}\rangle_y$, periodically producing an entangled GHZ state (*29*). Many-body spin interactions of this kind are an important ingredient in the simulation of systems with strict symmetry requirements (*30*) or spin models exhibiting topological order (*31*). Measurements in other bases and simulations of nearest-neighbor and many-body interactions with a transverse field using more than 100 gates are presented in (*23*).

Figure 4A shows the observed dynamics of the four-spin state $|{\uparrow}{\uparrow}{\uparrow}{\uparrow}\rangle$ under a long-range Ising-type interaction. The rich structure of the dynamics reflects the increased complexity of the underlying Hamiltonian: Oscillation frequencies correspond to the energy gaps in the spectrum. This information can be extracted via a Fourier transform of the data (*23*). Specific energy gaps could be targeted by preparing superpositions of eigenstates via an initial quasi-adiabatic digital evolution (*10*). Figure 4B shows the observed dynamics for our largest simulation: a six-spin many-body interaction, which directly couples the states $|{\uparrow}{\uparrow}{\uparrow}{\uparrow}{\uparrow}{\uparrow}\rangle$ and $|{\downarrow}{\downarrow}{\downarrow}{\downarrow}{\downarrow}{\downarrow}\rangle$, periodically producing a maximally entangled GHZ state.

Direct quantification of simulation quality for more than two qubits is impractical via QPT: For three qubits, expectation values must be measured for 1728 experimental configurations, and this increases exponentially with qubit number ($\approx 3 \times 10^6$ for six qubits). However, the average process fidelity (F_p) can be bounded more efficiently (*32*). We demonstrate this for the three- and six-spin simulations of Figs. 3C and 4B, respectively. Bounds of $85(1)\% \leq F_p \leq 91(1)\%$ (three spins) and $56(1)\% \leq F_p \leq 77(1)\%$ (six spins) are obtained at $\phi = 0.25\ \pi$, with 40 and 512 experimental configurations, respectively (*23*). The largest system for which a process fidelity has previously been measured is three qubits (*33*). A different measure of process quality is given by the worst-case fidelity, over all input states, and may be better used to assess errors in future full-scale fault-tolerant simulations. Regardless of the measure used, the error in large-scale digital simulations built from finite-sized operations can be efficiently estimated. Each operation can be characterized with a finite number of measurements, then the error in any combination can be chained (*34*). To exploit this, the number of ionic qubits on which our many-qubit operators O_{2-4} can act must be restricted.

The dominant effect of experimental error can be seen in Figs. 3B and 4B: The dynamics damps as a result of decoherence processes. Laser frequency and ambient magnetic field fluctuations are far from the leading error source: In the absence of coherent operations, qubit lifetimes are more than an order of magnitude longer (coherence times ≈30 ms) than the duration of

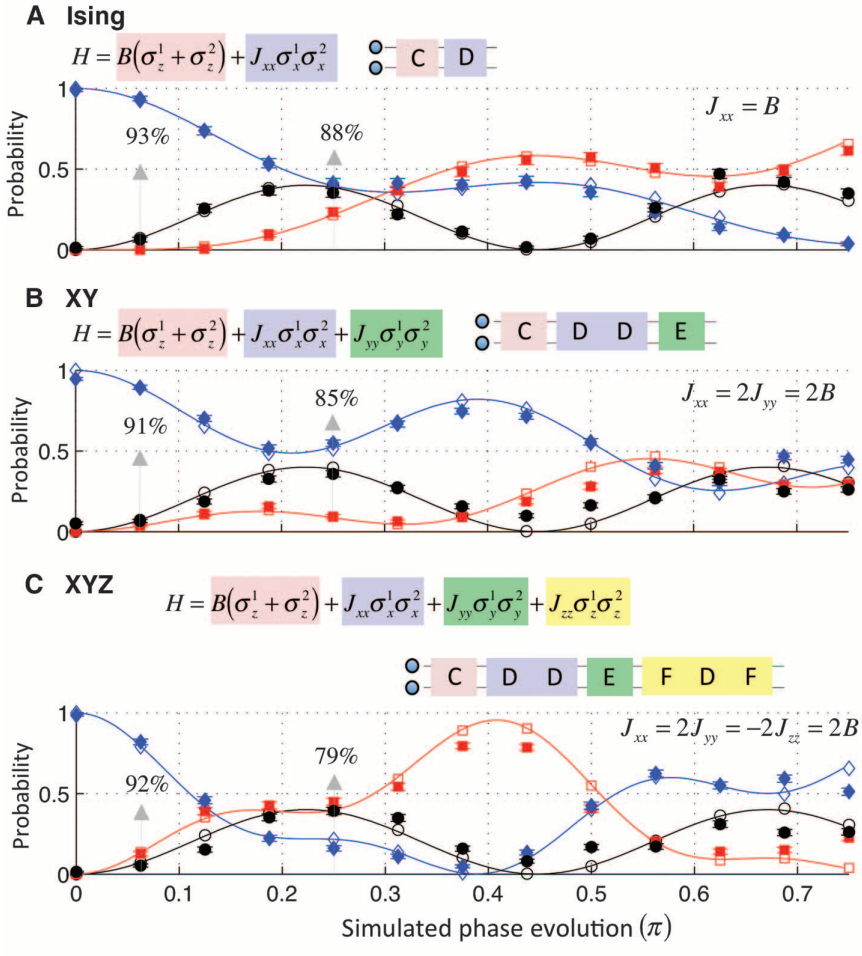

Fig. 2. (**A** to **C**) Digital simulations of increasingly complex two-spin systems. Dynamics of the initial state $|{\rightarrow}{\leftarrow}\rangle_x$ with a fixed digital resolution of $\pi/16$. The graphic in each panel shows how a single digital step is built: $C = O_2(\pi/16)$, $D = O_4(\pi/16,0)$, $E = O_4(\pi/16,\pi)$, $F = O_3(\pi/4,0)$. Quantum process fidelities between the measured and exact simulation after one and four digital steps are shown with gray arrows [uncertainties ≤ 1% (*23*)]. Lines; exact dynamics. Unfilled shapes: ideal digitized; filled shapes: data ($\blacklozenge{\rightarrow}{\leftarrow}_x$ $\blacksquare{\leftarrow}{\rightarrow}_x$ $\bullet{\leftarrow}{\leftarrow}_x$ or ${\rightarrow}{\rightarrow}_x$).

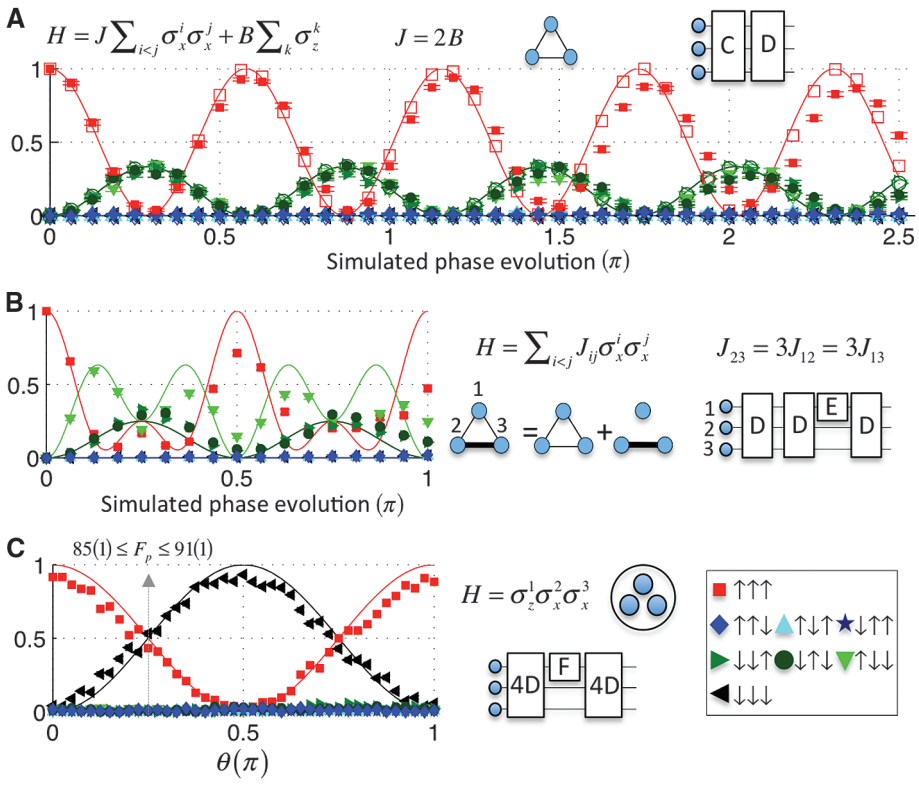

Fig. 3. Digital simulations of three-spin systems. Dynamics of the initial state $|\uparrow\uparrow\uparrow\rangle$ in three cases. (**A**) Long-range Ising system. Spin-spin coupling between all pairs with equal strength and a transverse field. $C = O_2(\pi/32)$, $D = O_4(\pi/16,0)$. (**B**) Inhomogeneous distribution of spin-spin couplings, decomposed into an equal-strength interaction and another with twice the strength between one pair. $E = O_1(\pi/2,1)$. (**C**) Three-body interaction, which couples the $\sum_j \sigma_y^j$ eigenstates $|\leftarrow\leftarrow\leftarrow\rangle_y$ and $|\rightarrow\rightarrow\rightarrow\rangle_y$. An $O_3(\pi/4,0)$ operation before measurement rotates the state into the logical σ_z basis. $F = O_1(\theta,1)$, $4D = O_4(\pi/4,0)$. Any point in the phase evolution is simulated by varying the phase θ of operation F. Inequalities bound the quantum process fidelity F_p [see (*23*) for details].

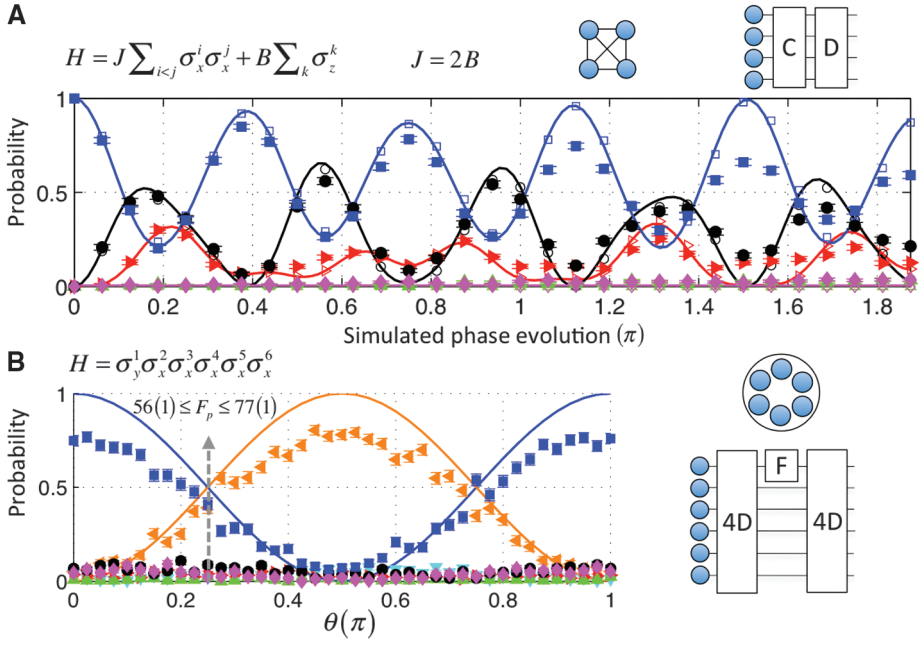

Fig. 4. Digital simulations of four and six spin systems. Dynamics of the initial state where all spins point up. (**A**) Four spin long-range Ising system. Each digital step is $D.C = O_4(\pi/16,0).O_2(\pi/32)$. Error bars are smaller than point size. (**B**) Six spin six-body interaction. $F = O_1(\theta,1)$, $4D = O_4(\pi/4,0)$. The inequality at $\phi = 0.25\ \pi$ bounds the quantum process fidelity F_p at $\theta = 0.25\ \pi$ [see (*23*) for details]. Lines; exact dynamics. Unfilled shapes: ideal digitized; filled shapes: data (■P_0 ◆P_1 ●P_2 ▲P_3 ►P_4 ▼P_5 ◄P_6, where P_i is the total probability of finding i spins pointing down).

experiments (≈1 to 2 ms). The current leading sources of error, which limit both the simulation complexity and size, are thought to be laser intensity fluctuations (*23*). This is not currently a fundamental limitation and, once properly addressed, should enable an increase in simulation capabilities.

The digital approach can be combined with existing tools and techniques for analog simulations to expand the range of systems that can be simulated. In light of the present work, and current ion trap development (*35*), digital quantum simulations involving many tens of qubits and hundreds of high-fidelity gates seems feasible in coming years.

References and Notes

1. R. P. Feynman, *Int. J. Theor. Phys.* **21**, 467 (1982).
2. I. Buluta, F. Nori, *Science* **326**, 108 (2009).
3. S. Somaroo, C. H. Tseng, T. F. Havel, R. Laflamme, D. G. Cory, *Phys. Rev. Lett.* **82**, 5381 (1999).
4. M. Greiner, O. Mandel, T. Esslinger, T. W. Hänsch, I. Bloch, *Nature* **415**, 39 (2002).
5. D. Leibfried *et al.*, *Phys. Rev. Lett.* **89**, 247901 (2002).
6. A. Friedenauer, H. Schmitz, J. T. Glueckert, D. Porras, T. Schaetz, *Nat. Phys.* **4**, 757 (2008).
7. R. Gerritsma *et al.*, *Nature* **463**, 68 (2010).
8. K. Kim *et al.*, *Nature* **465**, 590 (2010).
9. B. P. Lanyon *et al.*, *Nat. Chem.* **2**, 106 (2010).
10. K. R. Brown, R. J. Clark, I. L. Chuang, *Phys. Rev. Lett.* **97**, 050504 (2006).
11. J. T. Barreiro *et al.*, *Nature* **470**, 486 (2011).
12. J. Simon *et al.*, *Nature* **472**, 307 (2011).
13. R. Islam *et al.*, *Nat Commun* **2**, 377 (2011).
14. S. Lloyd, *Science* **273**, 1073 (1996).
15. E. Jane, G. Vidal, W. Dür, P. Zoller, J. I. Cirac, *Quantum Inf. Comput.* **3**, 15 (2003).

16. N. Wiebe, D. W. Berry, P. Hoyer, B. C. Sanders, http://arxiv.org/abs/1011.3489 (2010).
17. M. Nielsen, I. Chuang, *Quantum Computation and Quantum Information* (Cambridge Univ. Press, Cambridge, 2001).
18. A. Steane, *Nature* **399**, 124 (1999).
19. A. Auerbach, *Interacting Electrons and Quantum Magnetism* (Springer, New York, 1994).
20. P. Schindler *et al*., *Science* **332**, 1059 (2011).
21. H. F. Trotter, *Proc. Am. Math. Soc.* **10**, 545 (1959).
22. S. Lloyd, L. Viola, *Phys. Rev. A* **65**, 010101 (2001).
23. Materials and methods are available as supporting material on *Science* Online.
24. A. Sørensen, K. Mølmer, *Phys. Rev. Lett.* **82**, 1971 (1999).
25. J. Benhelm, G. Kirchmair, C. F. Roos, R. Blatt, *Nat. Phys.* **4**, 463 (2008).
26. D. Porras, J. I. Cirac, *Phys. Rev. Lett.* **92**, 207901 (2004).
27. J. F. Poyatos, J. I. Cirac, P. Zoller, *Phys. Rev. Lett.* **78**, 390 (1997).
28. A. G. White *et al*., *J. Opt. Soc. Am. B* **24**, 172 (2007).
29. W. Dür, G. Vidal, J. I. Cirac, *Phys. Rev. A* **62**, 062314 (2000).
30. I. Kassal, J. D. Whitfield, A. Perdomo-Ortiz, M.-H. Yung, A. Aspuru-Guzik, *Annu. Rev. Phys. Chem.* **62**, 185 (2011).
31. C. Nayak, S. H. Simon, A. Stern, M. Freedman, S. Das Sarma, *Rev. Mod. Phys.* **80**, 1083 (2008).
32. H. F. Hofmann, *Phys. Rev. Lett.* **94**, 160504 (2005).
33. T. Monz *et al*., *Phys. Rev. Lett.* **102**, 040501 (2009).
34. A. Gilchrist, N. K. Langford, M. A. Nielsen, *Phys. Rev. A* **71**, 062310 (2005).
35. J. P. Home *et al*., *Science* **325**, 1227 (2009).

Acknowledgments: We thank W. Dür, A. Aspuru-Guzik, and M. Brownnutt for discussions. We acknowledge financial support by the Austrian Science Fund (FWF) [SFB F40 FOQUS], the Institut für Quanteninformation GmbH, Intelligence Advanced Research Projects Activity, and the European Commission for support via the integrated project AQUTE, two Marie Curie International Incoming Fellowships, and the ERC advanced grant CRYTERION.

Supporting Online Material

www.sciencemag.org/cgi/content/full/science.1208001/DC1
SOM Text
Figs. S1 to S9
Tables S1 to S6
References

6 May 2011; accepted 14 July 2011
Published online 1 September 2011;
10.1126/science.1208001

Implementing the Quantum von Neumann Architecture with Superconducting Circuits

Matteo Mariantoni,[1,4]* H. Wang,[1]† T. Yamamoto,[1,2] M. Neeley,[1]‡ Radoslaw C. Bialczak,[1] Y. Chen,[1] M. Lenander,[1] Erik Lucero,[1] A. D. O'Connell,[1] D. Sank,[1] M. Weides,[1]§ J. Wenner,[1] Y. Yin,[1] J. Zhao,[1] A. N. Korotkov,[3] A. N. Cleland,[1,4] John M. Martinis[1,4]*

The von Neumann architecture for a classical computer comprises a central processing unit and a memory holding instructions and data. We demonstrate a quantum central processing unit that exchanges data with a quantum random-access memory integrated on a chip, with instructions stored on a classical computer. We test our quantum machine by executing codes that involve seven quantum elements: Two superconducting qubits coupled through a quantum bus, two quantum memories, and two zeroing registers. Two vital algorithms for quantum computing are demonstrated, the quantum Fourier transform, with 66% process fidelity, and the three-qubit Toffoli-class OR phase gate, with 98% phase fidelity. Our results, in combination especially with longer qubit coherence, illustrate a potentially viable approach to factoring numbers and implementing simple quantum error correction codes.

Quantum processors (*1*–*4*) based on nuclear magnetic resonance (*5*–*7*), trapped ions (*8*–*10*), and semiconducting devices (*11*) were used to realize Shor's quantum factoring algorithm (*5*) and quantum error correction (*6*, *8*). The quantum operations underlying these algorithms include two-qubit gates (*2*, *3*), the quantum Fourier transform (*7*, *9*), and three-qubit Toffoli gates (*10*, *12*). In addition to a quantum processor, a second critical element for a quantum machine is a quantum memory, which has been demonstrated, for example, using optical systems to map photonic entanglement into and out of atomic ensembles (*13*).

Superconducting quantum circuits (*14*) have met a number of milestones, including demonstrations of two-qubit gates (*15*–*20*) and the advanced control of both qubit and photonic quantum states (*19*–*22*). We demonstrate a superconducting integrated circuit that combines a processor—executing the quantum Fourier transform and a three-qubit Toffoli-class OR phase gate—with a memory and a zeroing register in a single device. This combination of a quantum central processing unit (quCPU) and a quantum random-access memory (quRAM), which comprise two key elements of a classical von Neumann architecture, defines our quantum von Neumann architecture.

In our architecture (Fig. 1A), the quCPU performs one-, two-, and three-qubit gates that process quantum information, and the adjacent quRAM allows quantum information to be written, read out, and zeroed. The quCPU includes two superconducting phase qubits (*18*, *19*, *21*, *22*), Q_1 and Q_2, connected through a coupling bus provided by a superconducting microwave resonator B. The quRAM comprises two superconducting resonators M_1 and M_2 that serve as quantum memories, as well as a pair of zeroing registers Z_1 and Z_2, two-level systems that are used to dump quantum information. The chip geometry is similar to that in (*21*, *22*), with the addition of the two zeroing registers. Figure 1B shows the characterization of the device by means of swap spectroscopy (*21*).

The computational capability of our architecture is displayed in Fig. 2A, where a seven-channel quantum circuit, yielding a 128-dimensional Hilbert space, executes a prototypical algorithm. First, we create a Bell state between Q_1 and Q_2 using a series of π-pulse, $\sqrt{\text{iSWAP}}$ (entangling state), and iSWAP (exchanging state) operations (step I, a to c) (*22*). The corresponding density matrix $\hat{\rho}_{(I)}$ [Fig. 2C (I)] is measured by quantum state tomography. The Bell state is then written into the quantum memories M_1 and M_2 by an iSWAP pulse (step II) (*22*), leaving the qubits in their ground states $|g\rangle$, with density matrix $\hat{\rho}_{(II)}$ [Fig. 2C (II)]. While storing the first Bell state in M_1 and M_2, a second Bell state with density matrix $\hat{\rho}_{(III)}$ [Fig. 2C (III)] is created between the qubits, using a sequence similar to the first operation (step III, a to c).

To reuse the qubits Q_1 and Q_2, for example to read out the quantum information stored in the memories M_1 and M_2, the second Bell state has to be dumped (*23*). This is accomplished using two zeroing gates, by bringing Q_1 on resonance with Z_1 and Q_2 with Z_2 for a zeroing time τ_z, corresponding to a full iSWAP (step IV). Figure 2B shows the corresponding dynamics, where each qubit, initially in the excited state $|e\rangle$, is measured in the ground state $|g\rangle$ after ≅ 30 ns. The density matrix $\hat{\rho}_{(IV)}$ of the zeroed two-qubit system is shown in Fig. 2C (IV). Once zeroed, the qubits can be used to read the memories (step V), allowing us to verify that, at the end of the algorithm, the stored state is still entangled. This is clearly demonstrated by the density matrix shown in Fig. 2C (V).

The ability to store entanglement in the memories, which are characterized by much longer coherence times than the qubits, is key to the quantum von Neumann architecture. We demonstrate this capability in Fig. 2, D and E, where the fidelity and concurrence metrics (*24*) of the Bell states stored in M_1 and M_2 are compared with

[1]Department of Physics, University of California, Santa Barbara, CA 93106–9530, USA. [2]Green Innovation Research Laboratories, NEC Corporation, Tsukuba, Ibaraki 305-8501, Japan. [3]Department of Electrical Engineering, University of California, Riverside, CA 92521, USA. [4]California NanoSystems Institute, University of California, Santa Barbara, CA 93106–9530, USA.

*To whom correspondence should be addressed. E-mail: matmar@physics.ucsb.edu (M.M.); martinis@physics.ucsb.edu (J.M.M.)

†Present address: Department of Physics, Zhejiang University, Hangzhou 310027, China.

‡Present address: Lincoln Laboratory, Massachusetts Institute of Technology, 244 Wood Street, Lexington, MA 02420–9108, USA.

§Present address: National Institute of Standards and Technology, Boulder, CO 80305, USA.